# Angle-resolved photoemission study of V-based kagome metal $CsV_8Sb_{12}$

Huan Ma,[1,2] Guohua Liu,[3] Liu Yang,[3] Qiangwei Yin,[1,2] Pengfei Ding,[1,2] Zhonghao Liu,[4,5] Hong-Yan Lu,[3,*] Hechang Lei,[1,2,†] and Shancai Wang[1,2,‡]

[1]*Department of Physics and Beijing Key Laboratory of Optoelectronic Functional Materials & Micro-Nano Devices, Renmin University of China, Beijing 100872, China*

[2]*Department of Physics, Key Laboratory of Quantum State Construction and Manipulation (Ministry of Education), Renmin University of China, Beijing 100872, China*

[3]*School of Physics and Physical Engineering, Qufu Normal University, Qufu 273165, China*

[4]*State Key Laboratory of Functional Materials for Informatics, Shanghai Institute of Microsystem and Information Technology, Chinese Academy of Sciences, Shanghai 200050, China*

[5]*College of Materials Science and Optoelectronic Technology, University of Chinese Academy of Sciences, Beijing 100049, China*

(Received 13 July 2023; revised 13 October 2023; accepted 8 November 2023; published 8 December 2023)

Recently, V-based kagome $AV_3Sb_5$ ($A$ = K, Rb, Cs) attracted researcher interest for the existence of charge-density wave (CDW), superconductivity, and nontrivial $\mathbb{Z}_2$ topological invariant. $CsV_8Sb_{12}$ has the same V-based kagome net, considered as the substitution of Cs with orthorhombic $V_2Sb_2$ layer. Using angle-resolved photoemission spectroscopy (ARPES) and density-functional theory (DFT), we find out that the symmetry of the Fermi surface (FS) and the electron structure near $E_F$ change from $C_6$ to $C_2$ symmetry. With the appearance of the electronic states from $V_2Sb_2$ layer near $E_F$, the corresponding bands from V-based kagome move to high binding energy by the introduction of $V_2Sb_2$ layer. We observe two types of saddle points. One at $\overline{\mathrm{M}}$ originates from the kagome lattice and locates at high binding energy. Another one at $\overline{\Gamma}$ arises from $V_2Sb_2$ layer and is situated near $E_F$. We study the influence of kagome distortion on the band structure using DFT, tight-binding model based on the ARPES experiment. We find that the $V_2Sb_2$-induced symmetry breaking and lattice distortion of the kagome net can lead to the shift of Dirac cones away from the high symmetry point. After considering spin-orbit coupling (SOC), the distorted kagome lattice shows the same topological properties as the pristine kagome lattice. Our findings will enhance comprehension of the microscopic mechanisms in V-based kagome metals and their topological properties.

DOI: 10.1103/PhysRevB.108.235129

## I. INTRODUCTION

The kagome lattice, a simple network composed of corner-sharing triangles, exhibits a wide range of phenomena [1]. By considering spins of localized electrons on the sites of the kagome lattice, one can realize a magnetic frustration-induced quantum spin liquid state [2]. On the other hand, by considering itinerant electrons among the sites of the kagome lattice, rich electronic structures can be obtained [3]. Typical electronic structures of the kagome lattice include the coexistence of flat bands, saddle points, and Dirac points. The enhanced density of states at the saddle points and the nesting of the FS near the van Hove filling promote electronic instabilities [4–6].

Recently, a family of V-based kagome compounds, denoted as $AV_3Sb_5$ ($A$ = K, Rb, Cs), with a nontrivial $\mathbb{Z}_2$ topological invariant has been discovered [7,8]. The $AV_3Sb_5$ mainly consists of a $V_3Sb_5$ layer sandwiched by an alkaline metal. In the $V_3Sb_5$ layer, V atoms form a two-dimensional (2D) kagome lattice. These $AV_3Sb_5$ materials undergo a charge-density wave (CDW) transition as the temperature decreases and exhibit superconductivity at low temperatures [9–11]. Phase transitions typically result in changes in symmetry, either structurally or electronically [12,13]. For example, $CsV_3Sb_5$ breaks the $C_6$ symmetry and exhibits a $2 \times 2$ charge modulation with a chiral charge order in the CDW phase, while it shows $C_2$ symmetry in its $c$-axis resistivity with an in-plane rotating magnetic field in the superconducting phase [14–19]. In the case of the double-layered V-based kagome material $CsV_6Sb_6$, Dirac nodal lines have been proposed, and a superconducting transition up to 1.48 K has been observed under high pressure [20].

Until recently, a new V-based kagome material $CsV_8Sb_{12}$ was discovered [21]. It is a quadruple-layered kagome metal formed by intercalating an orthorhombic $V_2Sb_2$ layer between two double $V_3Sb_5$ kagome layers. Despite its structural similarity to $CsV_3Sb_5$, $CsV_8Sb_{12}$ does not exhibit CDW or superconductivity down to 0.3 K under ambient pressure. However, it does display metallic and Pauli paramagnetic behaviors [21,22]. $CsV_8Sb_{12}$ features a staggered arrangement of the kagome layers along the $V_2Sb_2$ chain direction and an elongation of the $V_3Sb_5$ kagome structure along the same direction. The influence of these structural changes on the

*hylu@qfnu.edu.cn
†hlei@ruc.edu.cn
‡scw@ruc.edu.cn

 

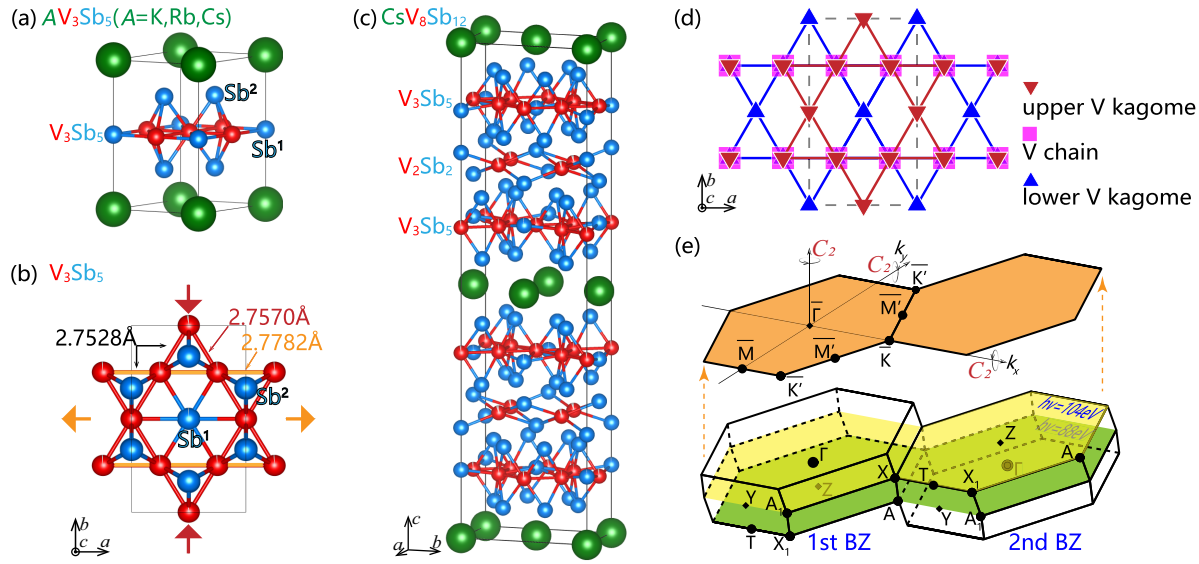


FIG. 1. (a) Crystal structure of $CsV_3Sb_5$ with space group $P6/mmm$ (No. 191). (b) Top view along the $c$ axis of $V_3Sb_5$ layer. V-V distance of $V_3Sb_5$ is denoted by black number in $CsV_3Sb_5$, while orange and red number in $CsV_8Sb_{12}$. Orange and red arrows show stretching and compression along the $a$ axis and $b$ axis, respectively. (c) Crystal structure of $CsV_8Sb_{12}$ with space group $Fmmm$ (No. 69), consisting of two sets of $V_3Sb_5$-$V_2Sb_2$-$V_3Sb_5$, namely kagome-chain-kagome structure. (d) Top view along the $c$ axis of V layers. The stacking order of kagome-chain-kagome structure is denoted as upper V kagome, V chain, lower V kagome. (e) First and second primitive BZs for $CsV_8Sb_{12}$. Yellow and green shaded areas represent $k_x$-$k_y$ planes at $k_z = 0, \pi$ recorded with $h\nu = 104, 88$ eV. Orange hexagon shaded areas shows the 2D BZ of the projected (001) surface.

band structure, topological properties, and their relationship to CDW and superconductivity in kagome materials remain open questions. In this study, we utilize ARPES measurements, DFT calculations, and a tight-binding model to investigate the electronic structure of the $CsV_8Sb_{12}$ kagome lattice and provide insights into these unresolved matters.

## II. METHODS

Single crystals of $CsV_8Sb_{12}$ were grown using self-flux method [21]. High-purity Cs (ingot), V (powder), and Sb (grain) were taken in a stoichiometric molar ratio of 1:8:50 for $CsV_8Sb_{12}$, and placed in a quartz tube with alumina crucible under partial argon atmosphere. The sealed quartz tubes for both materials were heated up to 1373 K for 12 h and soaked there for another 24 h. After that, for $CsV_8Sb_{12}$, the temperature was cooled down directly to 1123 K with the rate of 2 K/h. Finally, the ampoules were taken out of furnace and the single crystals were separated from the flux by a centrifuge. In order to prevent the reaction of Cs with air and water, all the preparation processes except the sealing and heat treatment procedures were carried out in an argon-filled glove box.

The ARPES experiments were performed on single crystals of $CsV_8Sb_{12}$. The samples were cleaved *in situ* in a vacuum better than $8 \times 10^{-11}$ Torr. ARPES measurements were performed at Dreamline and 09U beamlines of Shanghai Synchrotron Radiation Facility (SSRF). During measurements, the temperature was kept at $T = 10$ K, the pressure was better than $6 \times 10^{-11}$ Torr, and the energy resolution was set better than 15 meV.

The electronic structure was studied by the first-principles calculations with the projector-augmented wave (PAW) method [23,24] as implemented in the VASP package [25–27]. For the exchange-correlation function, the generalized gradient approximation (GGA) of the Perdew-Burke-Ernzerhof (PBE) formula [28] was adopted. The kinetic energy cutoff of the plane-wave basis was set to be 550 eV. A $5 \times 5 \times 18$ $k$-point mesh was utilized for the Brillouin zone (BZ) sampling and the Fermi surface (FS) was broadened by the Gaussian smearing method with a width of 0.05 eV.

The lattice parameters and internal atomic positions were fully relaxed until the forces on all atoms were smaller than 0.01 eV/Å. The crystal structure was visualized in the VESTA software [29]. The data of the orbital-projection band structure was processed by the VASPKIT software [30].

## III. CRYSTAL STRUCTURE

$CsV_8Sb_{12}$ crystallizes in an orthorhombic structure with No. 69 space group $Fmmm$ ($D_{2h}^{23}$) [21]. In contrast to $CsV_3Sb_5$, which consists of a single layer of kagome net [Fig. 1(a)], the unit cell of $CsV_8Sb_{12}$ contains four layers of $V_3Sb_5$ kagome nets and two layers of orthorhombic $V_2Sb_2$ nets [Fig. 1(c)]. Within a half unit cell, the kagome layers of $V_3Sb_5$ are separated by an orthorhombic $V_2Sb_2$ layer composed of two V chains. The two halves are separated by a Cs atom, resulting in the formation of the $CsV_8Sb_{12}$ unit cell. By examining the top view [Fig. 1(d)], it is evident that the two kagome layers are staggered by $a/2$ along the $a$ axis, which corresponds to the direction of the $V_2Sb_2$ chain.

In addition, the $V_3Sb_5$ kagome nets are compressed by $V_2Sb_2$ chains along the $b$ axis, resulting in the transformation of isosceles triangles to equilateral triangles with $d_{V-V} = 2.7782/2.7570$ Å, as shown in Fig. 1(b) [21]. This compression has the effect of slightly stretching or compressing the V-V bonds along the $a$ or $b$ directions, as indicated by the

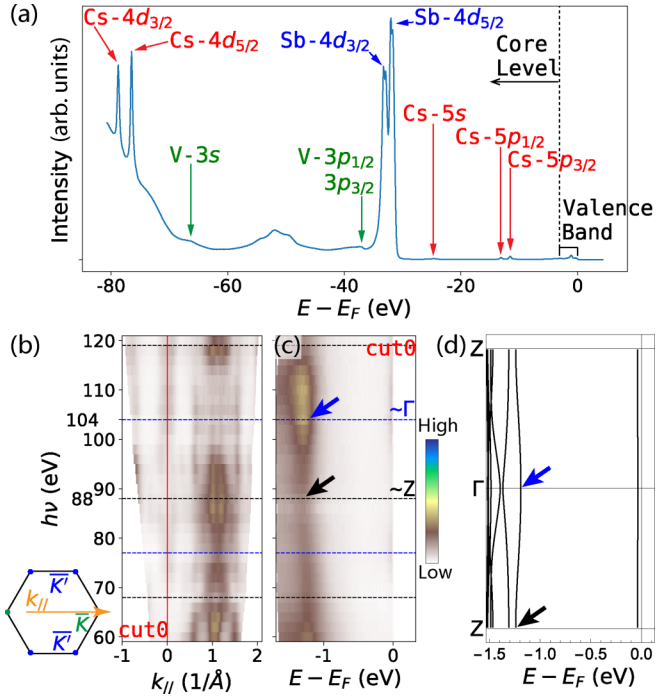


FIG. 2. (a) Core-level photoemission spectrum of $CsV_8Sb_{12}$ taken with $h\nu = 100$ eV. The total angular momentum quantum numbers are labeled for peaks. (b) The photon energy-$k_{//}$ intensity map along the $\overline{\Gamma}$-$\overline{K}$-$\overline{M}$ plane in BZ, marked by the orange arrow. (c) Photoemission intensity plot along cut0. (d) Band-structure calculation of $CsV_8Sb_{12}$ without SOC along Γ-Z.

orange/red colors in Fig. 1(b). The stacking arrangement of the kagome layers in $CsV_8Sb_{12}$ introduces a $C_2$ symmetry along the $c$ axis. As a result, the original $C_6$ symmetry of the BZ is broken, leading to a $C_2$ symmetry along the $k_z$ axis. Consequently, the $\overline{M}$ point becomes inequivalent to two $\overline{M}'$ points in the projected (001) surface BZ, as depicted in Fig. 1(e). The $\overline{K}$ and $\overline{K}'$ points also exhibit this inequivalence. Thus, the 2D BZ contains two types of high symmetry points: $\{\overline{M}, \overline{K}\}$ and $\{\overline{M}', \overline{K}'\}$.

## IV. FERMI SURFACE AND BAND DISPERSION

The core-level spectroscopy of $CsV_8Sb_{12}$ is shown in Fig. 2(a). The characteristic peaks of Cs-5$s$/5$p$/4$d$, V-3$s$/3$p$, and Sb-4$d$ orbitals in the core level region can be clearly observed. The high quality of the samples are characterized by the XRD and transport measurements in a separate paper [21].

By varying the photon energy from $h\nu = 60$ eV to 120 eV with a step size of 2 eV, a photon energy-$k_{//}$ intensity map is obtained and shown in Fig. 2(b), where $k_{//}$ is along the $\overline{\Gamma}$-$\overline{K}$-$\overline{M}$ direction in the BZ, as marked by the orange arrow in the inset of Fig. 2(b). The two-dimensional intensity map along $k_{//} = 0$ (cut0) is shown in Fig. 2(c). By combining the intensity map and plot along cut0 and the DFT calculations in Fig. 2(d), we confirmed that $h\nu = 104$ and 88 eV are near $k_z = 0, \pi$ planes, as indicated by the yellow and green shaded areas in Fig. 1(e), respectively. For simplicity, we use $\overline{\Gamma}$, $\overline{K}$, $\overline{K}'$, $\overline{M}$, and $\overline{M}'$ notations in the 2D BZ of the projected (001) surface, unless otherwise stated in the 3D BZ of $CsV_8Sb_{12}$.

The 2D intensity maps at $E_F$ (±15 meV) and 300 meV below $E_F$ of $k_z = 0$ and $k_z = \pi$ planes are shown in Figs. 3(a) and 3(b), respectively. Comparing the upper panels of Figs. 3(a) and 3(b), the Fermi surface (FS) topologies show similarities at these two $k_z$ planes, with variations in intensity due to matrix element effects. Along the $\overline{M}$-$\overline{\Gamma}$-$\overline{M}$ direction, the photoemission intensity shows an obvious braiding shape with a doubling of the periodicity, as shown in the upper panel of Figs. 3(a) and 3(b). From the figure, the FS exhibits a strong $C_2$ symmetry. This twofold rotational symmetry is more consistent with the orthorhombic $V_2Sb_2$ structure, suggesting that the electronic structures near $E_F$ are heavily influenced by the $V_2Sb_2$ chains. In the lower panel of Figs. 3(a) and 3(b), at high binding energy, the constant energy contour clearly exhibits a

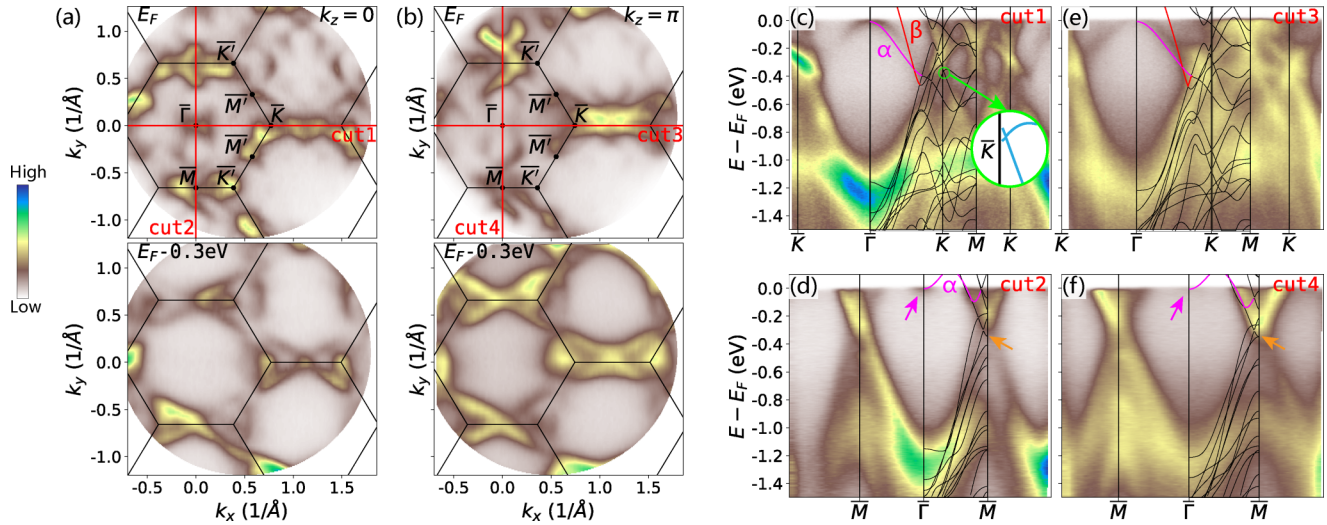


FIG. 3. Constant-energy intensity plots at binding energies of 0 and 0.3 eV at (a) $k_z = 0$ plane, and at (b) $k_z = \pi$ plane. The black solid lines indicate the 2D BZs. (c)−(f) Photoemission intensity plot along cut1 − 4 in (a) and (b). For comparison, the corresponding calculated bands (without SOC) are overlaid as black curves on top of the ARPES data.

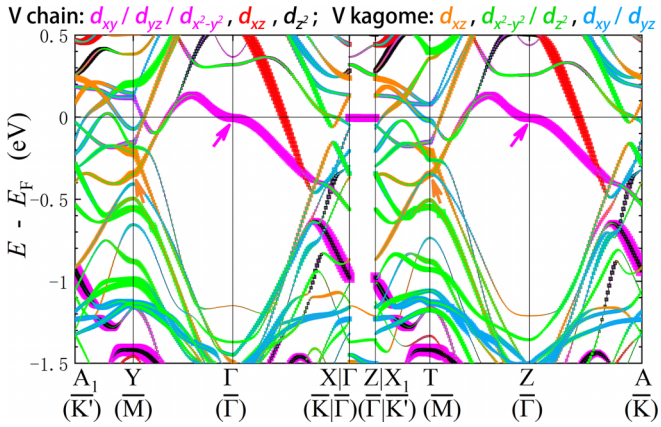


FIG. 4. Orbital projected band-structure calculation of $CsV_8Sb_{12}$ without SOC. The saddle points are indicated by the arrows.

$C_6$ symmetry. This reflects the feature of the kagome lattice layers and is similar to the FS topology of $CsV_3Sb_5$ [31].

We further investigate the electronic band structure along high symmetry lines (cut1 − 4) in Figs. 3(a) and 3(b). Along the high-symmetry line $\overline{\Gamma}$-$\overline{\mathrm{K}}$ in cut1 and cut3, one band ($\alpha$) approaches $E_F$ at $\Gamma$ while another band ($\beta$) crosses $E_F$ halfway between $\overline{\Gamma}$ and $\overline{\mathrm{K}}$. Along another high symmetry line $\overline{\Gamma}$-$\overline{\mathrm{M}}$ in cut2 and cut4, band $\alpha$ shows electronic behavior near $E_F$ around $\overline{\Gamma}$. Then band $\alpha$ turns back and crosses $E_F$ near the $\overline{\mathrm{M}}$ point. These two crossings correspond to the braiding-shaped FS, originating from the $d$ orbitals of V chains of the orthorhombic $V_2Sb_2$ layer according to the orbital projection of the bands shown in Fig. 4.

Additionally, the typical features of the electronic structure of the kagome lattice are investigated, including the flat band, Dirac cone, and saddle point. A near dispersionless peak with a weak intensity locates at high binding energy ($E_B \approx 1.1$ eV), which originates from the V kagome net. It hybridizes with several fast dispersive bands and becomes less noticeable. One flat feature at a binding energy around 0.4 eV, shown as cut3 in Fig. 3(e), is observed along $\overline{\mathrm{K}}$-$\overline{\mathrm{M}}$-$\overline{\mathrm{K}}$. At 0.4 eV below $E_F$ around $\overline{\mathrm{K}}$ point, Dirac-like crossing is predicated in DFT calculations, as indicated by the green circle in Fig. 3(c), and the corresponding linear dispersion around $\overline{\mathrm{K}}$ point is observed in the ARPES data in Figs. 3(c) and 3(e). However, due to the complex band structures of the double-layered V kagome lattices, several bands mix up and make the dispersion blurry around the $\overline{\mathrm{K}}$ point. Another feature is the saddle point. Comparing the ARPES data in Figs. 3(d) and 3(f) with the DFT calculations in Fig. 4, one saddle point is located around 0.4 eV below $E_F$ at $\overline{\mathrm{M}}$, as indicated by the orange arrow in the figures. In addition, there is another saddle point at the BZ center $\overline{\Gamma}$ near $E_F$, as pointed out by the magenta arrow in Figs. 3(d) and 3(f).

## V. SADDLE POINTS

The detailed band dispersion around two saddle points is shown in Fig. 5. Figures 5(a) and 5(e) depict the saddle point around $\overline{\mathrm{M}}$, exhibiting an electronlike dispersion $k_{//}^2$ along $\overline{\Gamma}$-$\overline{\mathrm{M}}$ and a holelike dispersion $-k_{\perp}^2$ along $\overline{\mathrm{M}}$-$\overline{\mathrm{K}}'$. When compared with the orbital-projection band-structure calculation in Fig. 4 (indicated by orange arrows), the saddle point at $\overline{\mathrm{M}}$ originates from the $d_{xz}$ orbitals of V kagome layers. If we take a closed

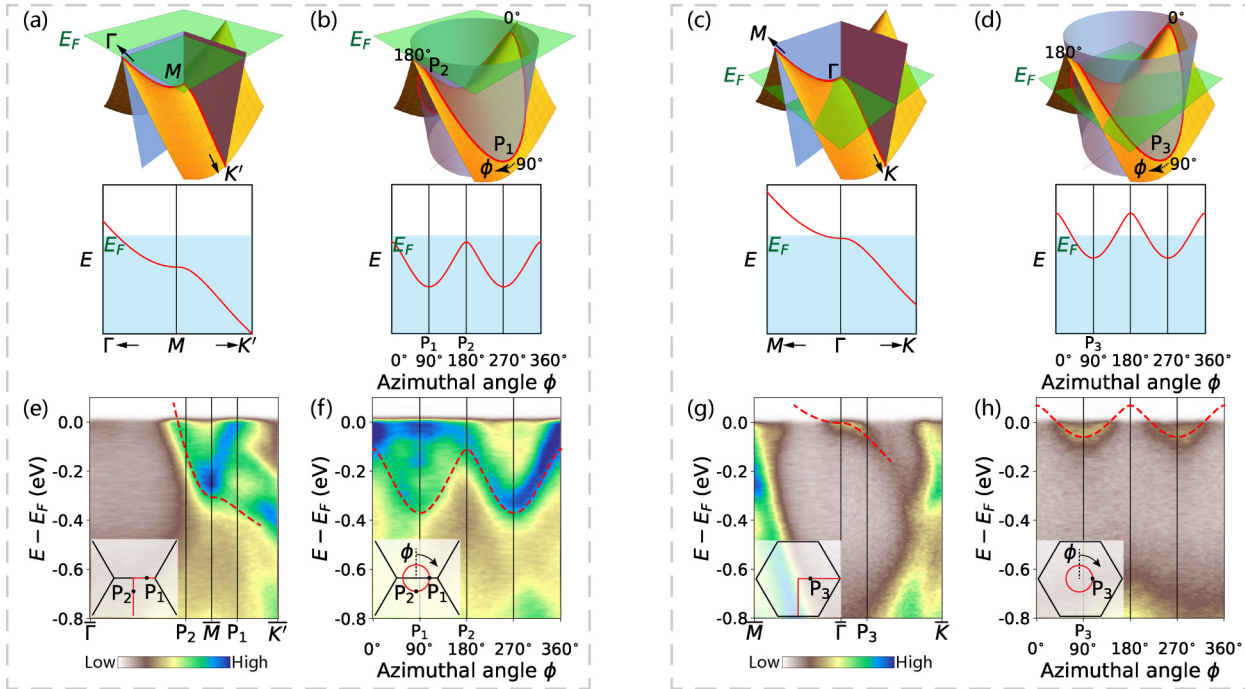


FIG. 5. 3D plots and band structures of the saddle points at high symmetry points, (a), (b) at M, and (c), (d) at Γ. Green plane indicates Fermi energy. The band dispersions in the lower panel correspond to intersection between light blue planes and 3D band dispersion, along various paths in the BZ. (e)−(h) Photoemission intensity plots of the corresponding red lines in (a)−(d). The momentum locations and the path are shown in the insets.

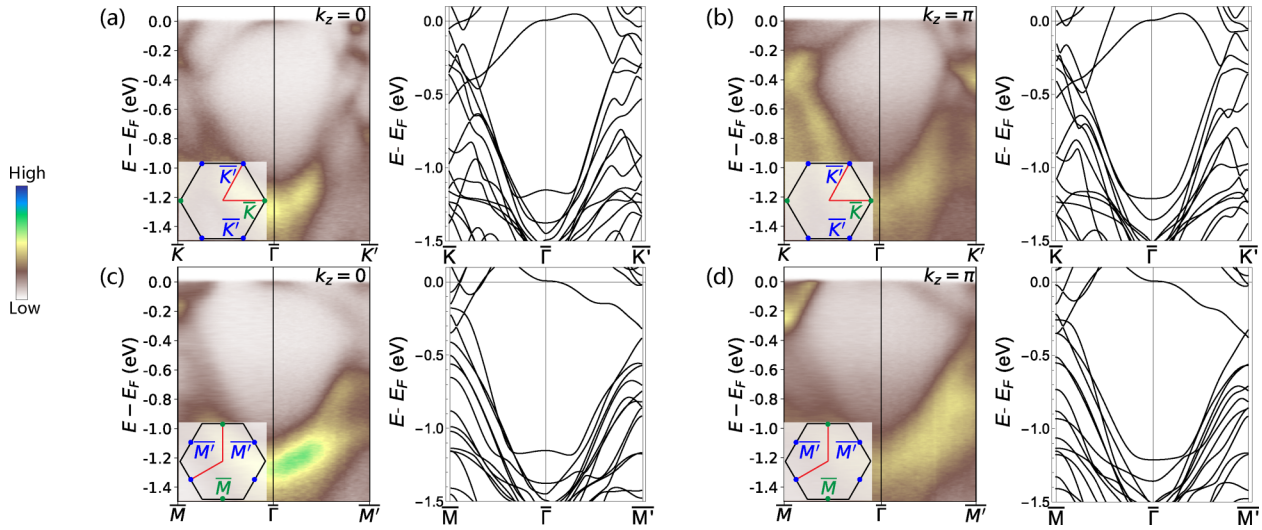


FIG. 6. Photoemission intensity plots and corresponding calculated band structures (without SOC) at (a), (c) $k_z = 0$ plane, and at (b), (d) $k_z = \pi$ plane. Paths are indicated by red lines in the inset of the BZ.

loop around $\overline{\text{M}}$, the band structure along this path exhibits a cosinelike curve, as indicated by the red intersection line between the light blue cylinder and the 3D band dispersion in Fig. 5(b). Figure 5(f) presents an intensity plot of the closed loop, showing a cosinelike band dispersion. The minimum and maximum points of the band dispersion are located at points $P_1$ and $P_2$, respectively, corresponding to $\phi = 90^\circ$ and $\phi = 180^\circ$ as indicated in the inset. Compared to $CsV_3Sb_5$, the saddle point of the V-based kagome is shifted to higher binding energy away from $E_F$ [31]. This downshift is caused by the introduction of the orthorhombic $V_2Sb_2$ layer. Additionally, the absence of van Hove singularities near $E_F$ could be related to the disappearance of CDW and superconductivity in kagome.

Another saddle point is located at the 2D BZ center, represented by $\overline{\Gamma}$, as shown in Figs. 5(c) and 5(g). The band dominantly exhibits an electronlike dispersion along the $\overline{\Gamma}$-$\overline{\text{M}}$ direction and a holelike dispersion along the $\overline{\Gamma}$-$\overline{\text{K}}$ direction. Comparing with the orbital-projection band-structure calculation in Fig. 4 (indicated by magenta arrows), the saddle point at $\overline{\Gamma}$ originates from the degenerate $d_{xy}$, $d_{yz}$, $d_{x^2-y^2}$ orbitals of the V chain. Similarly, we perform a closed-loop path centered around $\overline{\Gamma}$ and find a cosinelike band structure, as shown in Fig. 5(d). The minimum point of the band dispersion, corresponding to $P_3$, is located at $\phi = 90^\circ$, as indicated in the inset of Fig. 5(h). The saddle point around $\overline{\Gamma}$ close to $E_F$ enhances the density of states near $E_F$. However, being the only hot spot at the center of the BZ, the saddle point at $\overline{\Gamma}$ does not contribute to the intra-Fermi surface scattering.

## VI. KAGOME DISTORTION

The kagome lattice in $CsV_8Sb_{12}$ is compressed by the $V_2Sb_2$ layer along the $b$ axis. The degree of distortion in the kagome lattice, influenced by the interlayer coupling, is relatively high at 0.77% compared to the distortion rate achieved by uniaxial strain experiments [32]. This section investigates the influence of the kagome lattice distortion on the band structure using ARPES experiments, DFT calculations, and a tight-binding model.

To verify the presence of two types of inequivalent high symmetry points in the 2D BZ, we can compare the band structures along the $\overline{\Gamma}$-$\overline{\text{K}}$ and $\overline{\Gamma}$-$\overline{\text{K}}'$ paths, as well as the $\overline{\Gamma}$-$\overline{\text{M}}$ and $\overline{\Gamma}$-$\overline{\text{M}}'$ paths, respectively. We can observe the differences in band dispersion near the Fermi level ($E_F$) in these directions, as shown in Figs. 6(a) and 6(b) with ARPES intensity plots and corresponding calculated band structures (without SOC). At high binding energy $E_B > 0.5$ eV, the bands exhibit similar symmetry, except for subtle differences along these two directions. However, at low binding energy, the orbital contributions from the $d$ orbitals of the V chain in the $V_2Sb_2$ layer show a clear difference along these two paths. On the other hand, at higher binding energy, the bands are mainly influenced by the $d$ orbitals of the V kagome in the $V_3Sb_5$ layer due to the interlayer coupling between the V chain and the kagome lattice, as well as the kagome distortion. These bands exhibit quasi-$C_6$ symmetry. Similar behavior can be observed between the $\overline{\Gamma}$-$\overline{\text{M}}$ and $\overline{\Gamma}$-$\overline{\text{M}}'$ paths at the $k_z = 0$ and $k_z = \pi$ planes, as shown in Figs. 6(c) and 6(d).

After studying the effect of V chains and kagome distortion on the band structure, the next question arises: How does the band structure evolve when the primitive cell of the kagome lattice undergoes a transformation? In the case of $CsV_8Sb_{12}$, the equilateral triangle in the kagome lattice becomes an isosceles triangle. To investigate this, we compare the band structure calculations of $CsV_8Sb_{12}$ with a pristine kagome lattice (prime cell with an equilateral triangle shape) and a deformed kagome lattice (prime cell with an isosceles triangle shape), as shown in Fig. 7. Compared to the pristine kagome lattice, the electron bands originating from the $V_2Sb_2$ chain, which mainly localize at the BZ center, shift upward after the deformation. Conversely, the bands from the kagome layers shift downward. This causes an electron transfer from the $V_2Sb_2$ layer to the kagome layers. Moreover, the asymmetry between the $\overline{\Gamma}$-$\overline{\text{K}}$ and $\overline{\Gamma}$-$\overline{\text{K}}'$ (as well as the $\overline{\Gamma}$-$\overline{\text{M}}$ and $\overline{\Gamma}$-$\overline{\text{M}}'$) is further enhanced. A notable example is the flat band located 1.2 eV below $E_F$, indicated by the cyan rectangle in Fig. 7.

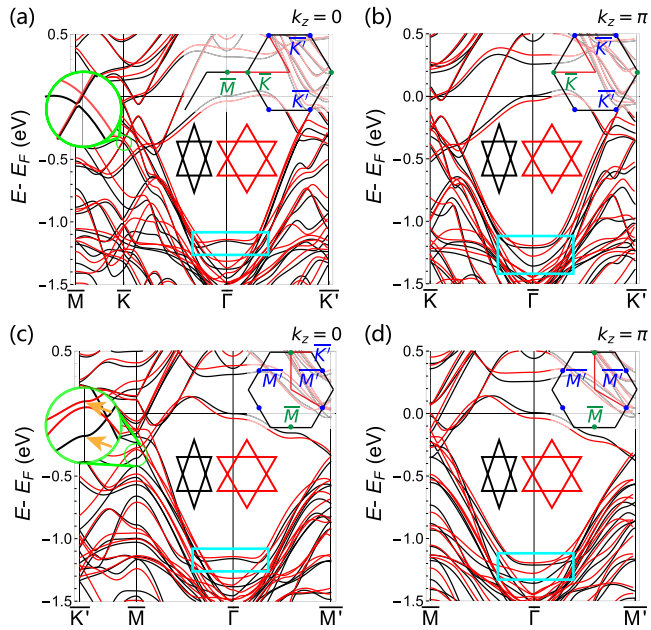


FIG. 7. Band-structure calculations without SOC at (a), (c) $k_z = 0$ plane, and at (b), (d) $k_z = \pi$ plane. $\overline{\text{M}}$-$\overline{\text{K}}$ in (a) is at $k_z = \pi$ plane of the extended 3D BZ. Paths are indicated by red lines in the inset. Stars of David with black and red colors indicate the deformed kagome (prime cell with an isosceles triangle shape) and pristine kagome (prime cell with an equilateral triangle shape in red curves), respectively.

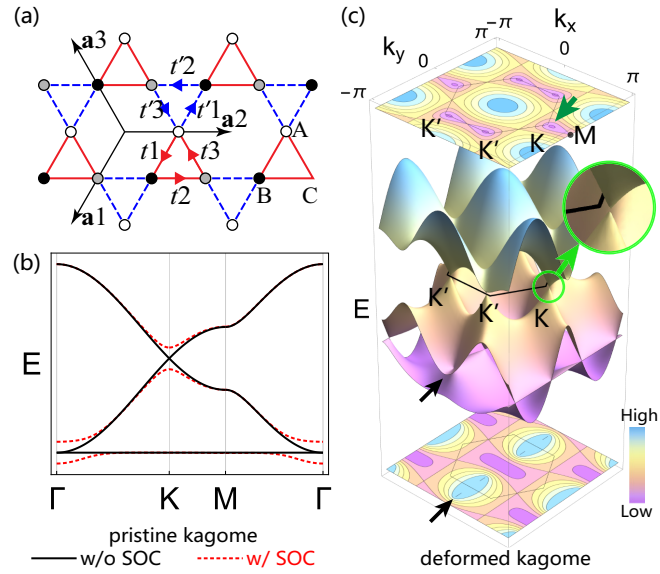


FIG. 8. (a) Kagome lattice with the definition of the lattice vectors $\mathbf{a}_{1,2,3}$. Upward triangulars (red solid lines) form primitive cells of kagome lattice with A, B, C sublattices (white, black, and gray dots). Downward triangulars (blue dashed lines) connect primitive cells. Red and blue arrows represent intra- and interprimitive-cell nearest-neighbor hopping, respectively. (b) Tight-binding band structure of the pristine kagome lattice without (black solid lines) and with (red dashed lines) SOC. (c) The band structure of deformed kagome lattice with $t_{1,3}/t_2 = t'_{1,3}/t'_2 = 3/2$. Top and bottom patterns of the box are contour plots of top and bottom band structures. Black solid lines represents BZs. Band crossing points are indicated by black and green arrows.

This band becomes more asymmetric along the $\overline{\text{K}}$-$\overline{\Gamma}$-$\overline{\text{K}'}$ (as well as $\overline{\text{M}}$-$\overline{\Gamma}$-$\overline{\text{M}'}$) directions. Saddle points around $\overline{\Gamma}$, as well as $\overline{\text{M}}$ indicated by the green circle in Fig. 7(c), shift slightly along the direction of the binding energy. Another significant change occurs in the Dirac cone at $\overline{\text{K}}$, indicated by the green circle and shown in the inset of Fig. 7(a). In a pristine kagome lattice, the crossing point is located at the high-symmetry point $\overline{\text{K}}$. However, after the deformation, the crossing point moves away from $\overline{\text{K}}$ towards $\overline{\text{M}}$ in the extended BZ.

In the kagome lattice, topological nontrivial properties occur due to the introduction of spin-orbit interaction [33–35]. It has been predicted that introducing a weak perturbation, such as a breathing deformation, to the kagome lattice can result in a diverse and rich phase diagram of its topological properties [36]. In this study, we employ a tight-binding model to investigate the effects of a deformed kagome lattice on $CsV_8Sb_{12}$ [37]. Considering a real-number nearest-neighbor (NN) hopping, the spinless Hamiltonian of the kagome lattice is written as

$$\begin{aligned}\mathcal{H}_0 = &\sum_{\mathbf{R}}[t_1 c^\dagger_{\mathbf{R},B} c_{\mathbf{R},A} + t_2 c^\dagger_{\mathbf{R},C} c_{\mathbf{R},B} + t_3 c^\dagger_{\mathbf{R},A} c_{\mathbf{R},C}] \\ &+ \sum_{\mathbf{R}}[t'_1 c^\dagger_{\mathbf{R}-\mathbf{a}_1,B} c_{\mathbf{R},A} + t'_2 c^\dagger_{\mathbf{R}-\mathbf{a}_2,C} c_{\mathbf{R},B} + t'_3 c^\dagger_{\mathbf{R}-\mathbf{a}_3,A} c_{\mathbf{R},C}] \\ &+ \text{H.c.}, \end{aligned} \tag{1}$$

where $c^\dagger_{\mathbf{R},\alpha}/c_{\mathbf{R},\alpha}$ creates/annihilates an electron on the sublattice $\alpha \in \{\text{A, B, C}\}$ of the primitive cell $\mathbf{R}$. The first and second terms are the hopping within a primitive cell $t_i$ and between two primitive cells $t'_i$. The NN hopping parameters $\{t_i\}_{i=1,2,3}$, $\{t'_i\}_{i=1,2,3}$ corresponds to upward and downward triangles in Fig. 8(a), respectively. H.c. stands for Hermitian conjugate.

To simplify the analysis, we set the hopping parameters as $t_{1,3}/t_2 = t'_{1,3}/t'_2 = 3/2$. Figure 8(c) displays the three-dimensional band dispersion, as well as the contour plots of the upper branch and the flat bands. As a reference, we compare these results with the band structures of the pristine kagome lattice shown in Fig. 8(b). It is observed that the crossing point of the Dirac dispersion deviates from the high-symmetry point K, as indicated by the green arrows and shown in the inset of the green circle in Fig. 8(c). This deviation is a consequence of the broken $C_3$ symmetry at that point. Moreover, the flat band exhibits dispersion and hybridization with other dispersive bands, as indicated by the black arrows in Fig. 8(c). In addition, the contour plots of both the upper band and the flat band reveal a distinct $C_2$ symmetry, rather than the $C_6$ symmetry observed in a pristine kagome lattice.

We further compare the band dispersion along high-symmetry lines with the pristine kagome lattice in Fig. 9. The upper and lower rows of the figure display the calculations for the pristine and deformed kagome structures, respectively. In the pristine kagome lattice, as shown in Fig. 9(a), the band dispersions exhibit symmetry along the Γ-K and Γ-K′ directions (as well as the Γ-M and Γ-M′ directions). However, with deformation, as depicted in Fig. 9(d), the band dispersions show asymmetric behavior along these two directions. The Dirac crossing point moves away from the

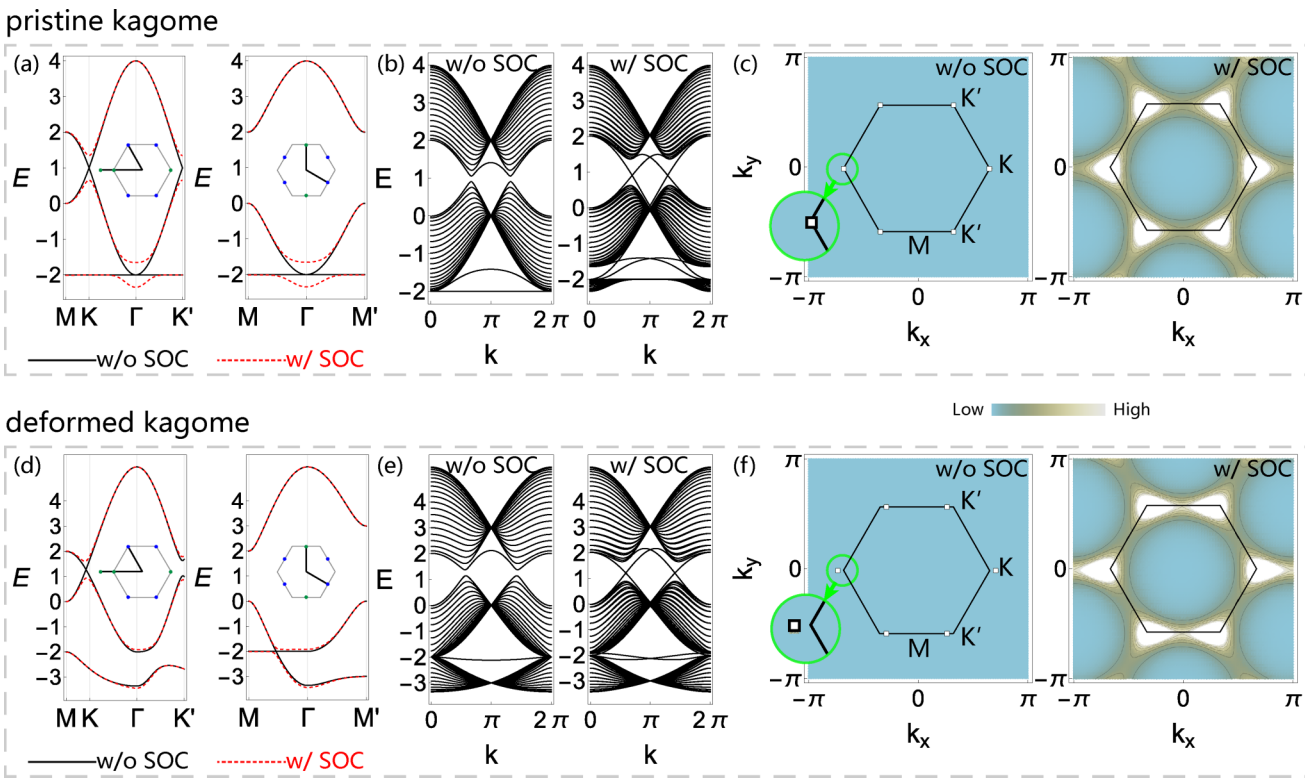


FIG. 9. Tight-binding model of (a)−(c) pristine kagome lattice $t_{1,2,3}/t'_{1,2,3} = 1$, and (d)−(f) deformed kagome lattice $t_{1,3}/t_2 = t'_{1,3}/t'_2 = 3/2$. The band structure along high-symmetry lines without and with SOC are presented with black solid lines and red dashed lines, respectively. (b), (e) The band structure of a system with edges of finite size along the $\mathbf{a}_1$ direction in prime cell coordinates, without (left panel) and with (right panel) SOC. (c), (f) Distribution of the Berry curvature for the upper branch of the Dirac cone, without (left panel) and with (right panel) SOC. The singularity point is prominently featured and indicated by the green circles in the zoomed-in view.

high-symmetry point K towards M in the extended BZ. Simultaneously, it also moves away from K′, resulting in a gap at this point. This tight-binding model provides an intuitive representation of the asymmetry in band dispersion and the shift of Dirac cones from high-symmetry points after deformation, consistent with the results of the DFT calculations shown in Fig. 7. The flat band also hybridizes with the dispersive band along the Γ-M direction and acquires dispersion. In the presence of SOC, the crossing points at these locations open up gaps.

Figures 9(b) and 9(e) present edge-state calculations for a finite-size system along the $\mathbf{a_1}$ direction for both the pristine and deformed lattices. In the absence of SOC, both cases exhibit trivial edge states. However, when SOC is taken into account, nontrivial edge states emerge in both the pristine and deformed cases. This indicates that the topological properties remain robust even in the presence of lattice deformation.

Significantly, the locations of the Berry curvatures undergo significant changes. In the pristine kagome lattice, the singularity of the Berry curvature is situated at the high-symmetry point K, as depicted by the green circle in Fig. 9(c). With deformation, it shifts away from K along the $k_x$ direction towards M in the extended Brillouin zone, as illustrated in Fig. 9(f). Consequently, the distribution of Berry curvatures exhibits $C_2$ symmetry [38]. When SOC is considered, the Berry curvature singularities become broader, but they still maintain clear $C_2$ symmetry.

## VII. CONCLUSION

In summary, by combining ARPES and DFT, we observe that the band-structure features of V-based kagome in $CsV_8Sb_{12}$ move to high binding energy with the introduction of orthorhombic $V_2Sb_2$ layer. We identify two types of saddle points: one located at $\overline{\mathrm{M}}$ formed by the kagome lattice, and another near the $\overline{\Gamma}$ point, formed by the $V_2Sb_2$ chain, close to the Fermi energy ($E_F$). Furthermore, we find that the distortion of the kagome lattice, caused by the presence of the $V_2Sb_2$ chain, results in a breaking of the $C_6$ symmetry in $CsV_8Sb_{12}$. Using the tight-binding model, we determined that the location of the Berry curvature singularity moves away from the high-symmetry points due to this distortion. However, the edge-state calculation suggests that nontrivial topological properties are not affected by the distortion of the kagome lattice.

The discovery of new V-based kagome metals of $CsV_8Sb_{12}$, as well as $CsV_6Sb_6$, proves the structural flexibility of V-based kagome metals. By introducing an intercalation layer, it could make an ideal 2D kagome net to study the typical band structure of kagome material. With intercalation of charge carrier, the typical band structure could be tuned to $E_F$ to drive many instabilities, such as magnetism, CDW, and superconductivity. The $CsV_8Sb_{12}$ provides a platform to study the the correlated properties of kagome with rich phases and instabilities.

## ACKNOWLEDGMENTS

This work is supported by the National Key Research and Development Program of China (Grant No. 2022YFA1403803) and the National Natural Science Foundation of China (Grant No. 12274455). H.M. is supported by the Fundamental Research Funds for the Central Universities, and the Research Funds of Renmin University of China (Grant No. 22XNH099). H.C.L. was supported by National Key R & D Program of China (Grants No. 2018YFE0202600 and No. 2022YFA1403800), Beijing Natural Science Foundation (Grant No. Z200005), National Natural Science Foundation of China (Grant No. 12174443), Beijing National Laboratory for Condensed Matter Physics, and Collaborative Research Project of Laboratory for Materials and Structures, Institute of Innovative Research, Tokyo Institute of Technology. H.Y.L. is supported by the National Natural Science Foundation of China (Grant No. 12074213), the Major Basic Program of Natural Science Foundation of Shandong Province (Grant No. ZR2021ZD01), and the Project of Introduction and Cultivation for Young Innovative Talents in Colleges and Universities of Shandong Province. Z.H.L. is supported by the National Natural Science Foundation of China (Grant No. 12222413) and the Natural Science Foundation of Shanghai (Grants No. 23ZR1482200 and No. 22ZR1473300).



[1] M. Mekata, Kagome: The story of the basketweave lattice, Phys. Today **56**, 12 (2003).

[2] Y. Zhou, K. Kanoda, and T.-K. Ng, Quantum spin liquid states, Rev. Mod. Phys. **89**, 025003 (2017).

[3] Z. Liu, F. Liu, and Y.-S. Wu, Exotic electronic states in the world of flat bands: From theory to material, Chin. Phys. B **23**, 077308 (2014).

[4] M. L. Kiesel, C. Platt, and R. Thomale, Unconventional fermi surface instabilities in the kagome Hubbard model, Phys. Rev. Lett. **110**, 126405 (2013).

[5] W.-S. Wang, Z.-Z. Li, Y.-Y. Xiang, and Q.-H. Wang, Competing electronic orders on kagome lattices at van Hove filling, Phys. Rev. B **87**, 115135 (2013).

[6] S.-L. Yu and J.-X. Li, Chiral superconducting phase and chiral spin-density-wave phase in a Hubbard model on the kagome lattice, Phys. Rev. B **85**, 144402 (2012).

[7] B. R. Ortiz, L. C. Gomes, J. R. Morey, M. Winiarski, M. Bordelon, J. S. Mangum, I. W. H. Oswald, J. A. Rodriguez-Rivera, J. R. Neilson, S. D. Wilson, E. Ertekin, T. M. McQueen, and E. S. Toberer, New kagome prototype materials: Discovery of $KV_3Sb_5$, $RbV_3Sb_5$, and $CsV_3Sb_5$, Phys. Rev. Mater. **3**, 094407 (2019).

[8] Y. Fu, N. Zhao, Z. Chen, Q. Yin, Z. Tu, C. Gong, C. Xi, X. Zhu, Y. Sun, K. Liu, and H. Lei, Quantum transport evidence of topological band structures of kagome superconductor $CsV_3Sb_5$, Phys. Rev. Lett. **127**, 207002 (2021).

[9] B. R. Ortiz, P. M. Sarte, E. M. Kenney, M. J. Graf, S. M. L. Teicher, R. Seshadri, and S. D. Wilson, Superconductivity in the $\mathbb{Z}_2$ kagome metal $KV_3Sb_5$, Phys. Rev. Mater. **5**, 034801 (2021).

[10] Q. Yin, Z. Tu, C. Gong, Y. Fu, S. Yan, and H. Lei, Superconductivity and normal-state properties of kagome metal $RbV_3Sb_5$ single crystals, Chin. Phys. Lett. **38**, 037403 (2021).

[11] B. R. Ortiz, S. M. L. Teicher, Y. Hu, J. L. Zuo, P. M. Sarte, E. C. Schueller, A. M. M. Abeykoon, M. J. Krogstad, S. Rosenkranz, R. Osborn, R. Seshadri, L. Balents, J. He, and S. D. Wilson, $CsV_3Sb_5$: A $\mathbb{Z}_2$ Topological kagome metal with a superconducting ground state, Phys. Rev. Lett. **125**, 247002 (2020).

[12] L. D. Landau, On the theory of phase transitions. I, in *Collected papers of L.D. Landau*, edited by D. Ter Haar (Pergamon, 1965), pp. 193–216.

[13] V. L. Ginzburg and L. D. Landau, On the theory of superconductivity, in *Collected papers of L.D. Landau*, edited by D. Ter Haar (Pergamon, 1965), pp. 217–225.

[14] N. Ratcliff, L. Hallett, B. R. Ortiz, S. D. Wilson, and J. W. Harter, Coherent phonon spectroscopy and interlayer modulation of charge density wave order in the kagome metal $CsV_3Sb_5$, Phys. Rev. Mater. **5**, L111801 (2021).

[15] Z. X. Wang, Q. Wu, Q. W. Yin, C. S. Gong, Z. J. Tu, T. Lin, Q. M. Liu, L. Y. Shi, S. J. Zhang, D. Wu, H. C. Lei, T. Dong, and N. L. Wang, Unconventional charge density wave and photoinduced lattice symmetry change in the kagome metal $CsV_3Sb_5$ probed by time-resolved spectroscopy, Phys. Rev. B **104**, 165110 (2021).

[16] Z. Wang, Y.-X. Jiang, J.-X. Yin, Y. Li, G.-Y. Wang, H.-L. Huang, S. Shao, J. Liu, P. Zhu, N. Shumiya, M. S. Hossain, H. Liu, Y. Shi, J. Duan, X. Li, G. Chang, P. Dai, Z. Ye, G. Xu, Y. Wang *et al.*, Electronic nature of chiral charge order in the kagome superconductor $CsV_3Sb_5$, Phys. Rev. B **104**, 075148 (2021).

[17] H. Li, S. Wan, H. Li, Q. Li, Q. Gu, H. Yang, Y. Li, Z. Wang, Y. Yao, and H.-H. Wen, No observation of chiral flux current in the topological kagome metal $CsV_3Sb_5$, Phys. Rev. B **105**, 045102 (2022).

[18] S. Ni, S. Ma, Y. Zhang, J. Yuan, H. Yang, Z. Lu, N. Wang, J. Sun, Z. Zhao, D. Li, S. Liu, H. Zhang, H. Chen, K. Jin, J. Cheng, L. Yu, F. Zhou, X. Dong, J. Hu, H.-J. Gao *et al.*, Anisotropic superconducting properties of kagome metal $CsV_3Sb_5$, Chin. Phys. Lett. **38**, 057403 (2021).

[19] Y. Xiang, Q. Li, Y. Li, W. Xie, H. Yang, Z. Wang, Y. Yao, and H.-H. Wen, Twofold symmetry of c-axis resistivity in topological kagome superconductor $CsV_3Sb_5$ with in-plane rotating magnetic field, Nat. Commun. **12**, 6727 (2021).

[20] M. Shi, F. Yu, Y. Yang, F. Meng, B. Lei, Y. Luo, Z. Sun, J. He, R. Wang, Z. Jiang, Z. Liu, D. Shen, T. Wu, Z. Wang, Z. Xiang, J. Ying, and X. Chen, A new class of bilayer kagome lattice compounds with Dirac nodal lines and pressure-induced superconductivity, Nat. Commun. **13**, 2773 (2022).

[21] Q. Yin, Z. Tu, C. Gong, S. Tian, and H. Lei, Structures and physical properties of V-based kagome metals $CsV_6Sb_6$ and $CsV_8Sb_{12}$, Chin. Phys. Lett. **38**, 127401 (2021).

[22] Y. Yang, W. Fan, Q. Zhang, Z. Chen, X. Chen, T. Ying, X. Wu, X. Yang, F. Meng, G. Li, S. Li, L. Gu, T. Qian, A. P. Schnyder, J. gang Guo, and X. Chen, Discovery of two families of Vsb-based compounds with v-kagome lattice, Chin. Phys. Lett. **38**, 127102 (2021).

[23] P. E. Blöchl, Projector augmented-wave method, Phys. Rev. B **50**, 17953 (1994).

[24] G. Kresse and D. Joubert, From ultrasoft pseudopotentials to the projector augmented-wave method, Phys. Rev. B **59**, 1758 (1999).

[25] G. Kresse and J. Hafner, *Ab initio* molecular dynamics for liquid metals, Phys. Rev. B **47**, 558 (1993).

[26] G. Kresse and J. Furthmüller, Efficiency of *ab-initio* total energy calculations for metals and semiconductors using a plane-wave basis set, Comput. Mater. Sci. **6**, 15 (1996).

[27] G. Kresse and J. Furthmüller, Efficient iterative schemes for *ab initio* total-energy calculations using a plane-wave basis set, Phys. Rev. B **54**, 11169 (1996).

[28] J. P. Perdew, K. Burke, and M. Ernzerhof, Generalized gradient approximation made simple, Phys. Rev. Lett. **77**, 3865 (1996).

[29] K. Momma and F. Izumi, VESTA 3 for three-dimensional visualization of crystal, volumetric and morphology data, J. Appl. Crystallogr. **44**, 1272 (2011).

[30] V. Wang, N. Xu, J.-C. Liu, G. Tang, and W.-T. Geng, VASPKIT: A user-friendly interface facilitating high-throughput computing and analysis using VASP code, Comput. Phys. Commun. **267**, 108033 (2021).

[31] R. Lou, A. Fedorov, Q. Yin, A. Kuibarov, Z. Tu, C. Gong, E. F. Schwier, B. Büchner, H. Lei, and S. Borisenko, Charge-density-wave-induced peak-dip-hump structure and the multiband superconductivity in a kagome superconductor $CsV_3Sb_5$, Phys. Rev. Lett. **128**, 036402 (2022).

[32] T. Qian, M. H. Christensen, C. Hu, A. Saha, B. M. Andersen, R. M. Fernandes, T. Birol, and N. Ni, Revealing the competition between charge density wave and superconductivity in $CsV_3Sb_5$ through uniaxial strain, Phys. Rev. B **104**, 144506 (2021).

[33] F. D. M. Haldane, Model for a quantum Hall effect without landau levels: Condensed-matter realization of the "parity anomaly", Phys. Rev. Lett. **61**, 2015 (1988).

[34] C. L. Kane and E. J. Mele, Quantum spin Hall effect in graphene, Phys. Rev. Lett. **95**, 226801 (2005).

[35] D.-S. Ma, Y. Xu, C. S. Chiu, N. Regnault, A. A. Houck, Z. Song, and B. A. Bernevig, Spin-orbit-induced topological flat bands in line and split graphs of bipartite lattices, Phys. Rev. Lett. **125**, 266403 (2020).

[36] A. Bolens and N. Nagaosa, Topological states on the breathing kagome lattice, Phys. Rev. B **99**, 165141 (2019).

[37] H.-M. Guo and M. Franz, Topological insulator on the kagome lattice, Phys. Rev. B **80**, 113102 (2009).

[38] E. Tang, J.-W. Mei, and X.-G. Wen, High-temperature fractional quantum Hall states, Phys. Rev. Lett. **106**, 236802 (2011).